Journal of King Saud University – Engineering Sciences 34 (2022) 350–360

Contents lists available at ScienceDirect

Journal of King Saud University – Engineering Sciences

journal homepage: www.sciencedirect.com

Original article

Entrance and exit effects on oscillatory flow within parallel-plates in standing-wave thermoacoustic system with two different operating frequencies

Waleed Almukhtar Allafi [a], Fatimah Al Zahrah Mohd Saat [a,b,*]

[a] Fakulti Kejuruteraan Mekanikal, Universiti Teknikal Malaysia Melaka, Hang Tuah Jaya, 76100 Durian Tunggal, Melaka, Malaysia
[b] Centre for Advanced Research on Energy, Universiti Teknikal Malaysia Melaka, Hang Tuah Jaya, 76100 Durian Tunggal, Melaka, Malaysia

ARTICLE INFO

Article history:
Received 14 May 2020
Accepted 21 December 2020
Available online 31 December 2020

Keywords:
Entrance region
Oscillatory flow
Thermoacoustics
Flow frequency
Porous media

ABSTRACT

Thermoacoustics is about conversion between thermal and acoustical energies to provide alternative green technology for power cycle and cooling system. The oscillatory flow across porous structure inside the system is playing the role of energy conversion between the acoustic wave and the surface of the porous structure. Better understanding of fluid dynamics of oscillatory flow inside thermoacoustic system is therefore important for the thermoacoustic based energy conversion system. This paper presents the 'entrance' and 'exit' effects of the oscillatory flow within a parallel-plate structure that is placed inside a standing-wave thermoacoustic environment. Two-dimensional SST k-ω CFD models which were validated using experimental data and theoretical predictions were used for this investigation. Two different operating frequencies of 14.2 Hz and 23.6 Hz were studied for flow with five different amplitudes that were represented using drive ratios of 0.3%, 0.83%, 1.5%, 2.1% and 3%. These correspond to cases with Reynolds numbers between 5936 and 62926. Due to the cyclic nature of the flow, a region defined as an 'exit' region was observed in addition to the usual 'entrance' region and the fully developed region for flow inside a channel. The change of shape of velocity profiles from the 'm' shape profile, to the 'slug-like' profile and 'parabolic-like' profile was discussed in relation to the 'entrance' and 'exit' effects on flow inside the channel. The 'entrance' and 'exit' effects become bigger as drive ratio increases. The effect of 'entrance' and 'exit' are slightly reducing as frequency increases from 14.2 Hz to 23.6 Hz. This may be related to the shorter travel distance of fluid as the frequency increases. The results shown in this paper suggest that the flow within a 200 mm parallel-plate structure should be treated as developing flow especially for flow with low resonance frequency at drive ratio higher than 1%.

1. Introduction

The concern related to the impact of technological development on the sustainability and health of the environment had recently caught the attention of many researchers in the field of engineering and technology. Alternative technological solutions for electrical generator (Mazzetti et al., 2018; Gallego et al., 2020) as well as cooler (Brown and Domanski, 2014) have been reported by many with intentions of fulfilling the human needs without sacrificing the future of healthy environment. These include the use of thermoelectric principles (Al-habahbeh et al., 2018), thermoacoustics (Abdoulla-Latiwish and Jaworski, 2019) as well as solar energy (Homadi et al., 2020), just to name a few. In fact, some of these technologies are suitable to be applied for rural areas where access to electricity are limited (Gallego et al., 2020; Abdoulla-Latiwish and Jaworski, 2019). One of the alternative technologies that could be considered as a green technology is known as thermoacoustic technology. It can be used for power cycle (engine/generator) as well as a refrigeration cycle (refrigerator or heat pump). Thermoacoustic engines or acoustic heat engines are energy conversion devices that achieve simplicity and concomitant reliability by the use of acoustic technology. In thermoacoustic prime movers, heat that flows from a high-temperature source to a low-temperature sink generates acoustic power (which may be converted to electric

* Corresponding author.
E-mail address: fatimah@utem.edu.my (F.A.Z. Mohd Saat).
Peer review under responsibility of King Saud University.

Production and hosting by Elsevier

https://doi.org/10.1016/j.jksues.2020.12.008

Nomenclature

a	Speed of sound	X	Distance from the pressure antinode
C_p	Heat capacity (specific heat) at constant pressure	y	Space between the plates
D	gap between bottom and top walls of a channel	y_0	Half the plate spacing
Dr	Drive ratio	δ_k	Thermal penetration
f	Oscillation frequency	δ_v	Viscous penetration depth
g	Gravity = 9.81 m/s	ξ	Displacement
h_v	Shape factor	$\varnothing$	Porosity
k	Thermal conductivity	κ	Diffusivity of the gas
k_a	wave number	λ	Wavelength
ℓ	Turbulent length scale	μ	Dynamic viscosity
p_a	pressure at antinode	ω	Angular frequency
P_1	Oscillating pressure amplitude	ρ	Density
Re	Reynolds number	ρ_m	Mean density
r_h	Hydraulic radius	θ	Time phase
SST	Shear Stress Transport (turbulence k-ω model)	v	Kinematic viscosity
t	Time		
TI	Turbulence intensity		
U	Velocity amplitude		

power using a transducer) (Swift, 1988, 2002). Complex fluid flow and energy transfer interaction happens between an oscillatory flow and a solid material of an internal structure of the system during the operation of thermoacoustic device. The understanding of the flow behavior and heat transfer across the interior structure inside an oscillating fluid environment are one of the keys to a better design and development of thermoacoustic system (Swift, 2002; Agarwal et al., 2016).

In order to produce the thermodynamics processes of energy systems, thermoacoustic systems require the presence of several parts such as a porous structure known as 'stack'/'regenerator', a resonator that hold the soundwave, a heat exchanger to exchange heat with environment and the acoustic driver/loudspeaker/alternator to either drive the flow or convert the acoustic energy into electricity depending on whether the system is a generator or a cooler (Agarwal et al., 2016; Nakamura et al., 2017). Fig. 1 illustrates the principle concept of operation for the standing-wave thermoacoustic refrigerator system. The system is made of a resonator that contains a porous structure known as 'stack'. The stack is sandwiched between a hot heat exchanger and a cold heat exchanger. These structures are placed at a location inside the resonator where decent amount of the product of acoustic pressure and acoustic velocity can be achieved. Once the loudspeaker is turned on, an acoustic work ($\dot{W}$) creates the waves inside the

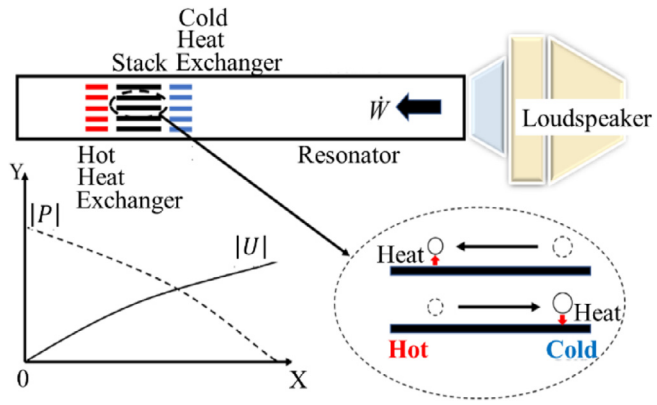

Fig. 1. Schematic diagram and basic operation principle of a standing-wave thermoacoustic refrigeration.

resonator and the parcels of the gas medium within the resonator start to oscillate forth and back. Consider one parcel of gas that is located near to the wall of the stack as shown in Fig. 1. The parcel moved to the left and right sides of the resonator following the oscillatory flow motion. As the parcel flows left, it is moving towards the higher-pressure region and be compressed adiabatically. This increases the pressure and temperature of the gas. The heated gar particle becomes hotter than the solid structure of the porous stack material and hence heat is transferred to the left end of the stack. Next, the gas oscillates back to the right side where the original place was. The parcel of gas is expanding adiabatically because it travels to an area with a lower pressure. The temperature also decreases as the pressure of the parcel is reduced. Finally, the temperature of parcel becomes lower than that of the solid, thus the heat is transferred from the solid to the parcel at constant pressure condition. These compression, expansion and heat transfer processes of gas parcel form a thermodynamic cycle in which the stack acts as sink and source in the terminal points of the movement of each parcel. Consequently, in each cycle of the sound wave, each gas parcel pumps a little amount of heat from the right of the stack to the left, from cold to hot. This thermodynamic process within the acoustic wave environment is commonly referred to as the "thermoacoustic effect" (Nakamura et al., 2017; Avent and Bowen, 2015).

Fluid dynamics behavior within the porous structure is playing important role in supporting the 'thermoacoustic effect' within the system. 'Entrance effects' may influence the behavior of an oscillatory flow induced by intersectional discontinuities such as 'stacks', 'regenerators' and 'heat exchangers', in a manner that is not well understood (Mao et al., 2007). An experimental study was used to demonstrate the thermoacoustic energy conversion phenomenon in a standing wave system (Harikumara et al., 2019). The stack was made from plastic straws and air was used as a working fluid. The system was driven at resonance frequency of 70 Hz with drive ratio bigger than 3%. In the experiment, the stack was placed at two positions: at the middle of the resonator and at a location towards the end of the resonator. The results showed that the stack at the middle of resonator was able to produce a temperature difference of 14.1 °C at drive ratio of 3.57%. When the stack moved nearer to the end of the resonator a lower temperature difference between the ends of the stack was recorded. In a different investigation, the velocity field inside an oscillating flow between the parallel plates of the 'stack' was

measured by using PIV (Nabavi et al., 2008; Berson et al., 2008). The results indicated that the generated vortex was attached to the plate at low flow amplitude. Whereas at high amplitude of flow the vortices detached from the plates. The behavior of vortex at both ends of the porous structure indicates a possibility of unique behavior of flow within the entrance region of the channel. Vortex shedding pattern at end of plates were also observed to change with plate thickness, spacing and drive ratio of the oscillating flow (Shi et al., 2011). The general trend of oscillating flow was observed for Reynolds ranging between 200 and 5000 using a Particle Image Velocimetry (PIV) method. The flow physics controlling the vortex shedding frequency in the "ejection" stage of the oscillation cycle was reported to be similar to that for steady flows. Investigations of entrance effect in the field of thermoacoustic is scarce but general understanding can be obtained through entrance region investigations in many different fields of study. In the classical approach, a hydrodynamic entry length in a rectangular channel was solved using a method of linearizing the Navier-Stokes equation (Han, 1960). The resulting equation was considered as a mathematical expression that represents the axial velocity in the whole region of the channel. The entire region was defined based on the entry length. The entry length for entrance region was defined at a location where 99% of the fully developed centerline velocity is reached. Comparison was also done between the entry length of oscillating flow and the entry length of the steady flow (Gerrard and Hughes, 1971). The results showed that the development of an oscillating flow in the entrance region of a pipe of circular cross-section is the same as it is for steady flow if the axial distance x from the entry is expressed as $xv/\delta^2 u_0$, where v is the kinematic viscosity coefficient, u_0 is the instantaneous entry velocity and δ is the oscillating boundary-layer thickness of the flow. The boundary layer thickness is the distance from the wall beyond which the velocity differs by less than 1% from the centerline velocity. In a different study, a laminar flow of a Newtonian fluid in the inlet of a circular pipe was analyzed numerically (Dombrowski et al., 1993). The range of Reynolds number was between 0 and 500 and the models were solved using a finite element based Computational Fluid Dynamics (CFD) code. It was found that a new flow phenomenon occurs at low Reynolds number <50. There was an existence of a peak in the axial pressure profile at a small distance from the entrance. The peak decreased by the increased of Reynolds number. This shows that the axial velocity profiles show concavity close to the entrance for all range of Reynolds used in the reported work. These concave profiles have been reported by other researchers both for circular tubes and parallel plates (Wang and Longwell, 1964; Gillis and Brandt, 1966; Friedmann et al., 1968). A steady entry flow was also studied for a case with an applied electrical potential through microchannels between two parallel plates (Yang et al., 2001). A nonlinear, two-dimensional Poisson equation and Zeta potential of the solid–liquid boundary and the Nernst-Plank equation were applied to investigate the impact of entry length on the fluid velocity distribution. The results showed that the entrance region of the electroosmotic flow is longer than that of classical pressure-driven flow. The thickness of the electrical double layer (EDL) in the entry region is thinner than that in the fully developed region. The change of velocity profile was also observed in the entry length. An experimental study of heat transfer of oscillatory flow across porous channel was conducted and the surface temperature distribution for the steady and oscillating flows were measured (Fu et al., 2001). The local and length-averaged Nusselt number were analyzed. The finding showed that the surface temperature distribution for the oscillating flow is more uniform than that for the steady flow. Two thermal entrance regions for the oscillating flow during reversing flow were detected. The maximum local temperature occurred at the center of the test section and the lower temperature was at the entrance regions. The length averaged Nusselt number of the oscillatory flow was found higher than that for the steady flow (Fu et al., 2001). An ultrasonic velocity profile (UVP) measurement method was used to investigate the "entry length" in oscillatory pipe flow (Yamanaka et al., 2002). The results showed that there was nonlinear oscillation of flow that occurred at the central area within the entrance region. The entry length of oscillating flow becomes longer when the boundary-layer thickness becomes thinner. This is different from the case of steady flow. Another experimental study of flow visualization within the entrance section of channels was conducted with sinusoidal plates placed in a water environment (Oviedo-Tolentino et al., 2008). A laser illuminated particle tracking was utilized as the technique of flow visualization. It was varied with the distance between plates, phase angle, and Reynolds number while the geometric parameters were kept constant. The flow regimes that were observed were steady, unsteady, and significant-mixed flows. The results showed that instabilities of the flow appeared near the exit of the channel and move closer to the inlet waves as Reynolds number grows. The first wave from the inlet showed that the flow was always steady. Unsteady behavior appeared when flow Reynolds number grew with the distance between plates. They suggested that the channel with eight waves long should be considered to develop the flow in a channel of this class. In a thermoacoustic field of study, an entrance effect investigation within a channel of a 'stack' was conducted by using data from Particle Image Velocimetry (PIV). The data was supported and supplemented by results from Computational Fluid Dynamics (CFD) method (Jaworski et al., 2009). They found that the velocity profile was never flat at the entry into the channel as was the case for piston-induced pipe flows. They proposed a method of investigating the entrance effects by monitoring velocity values in the centerline of the channel. In a different investigation, a three-dimensional direct numerical simulation (DNS) model of oscillatory pipe flows was investigated theoretically and experimentally (Feldmann and Wagner, 2012). The study was related to the transition to turbulence in Sexl-Womersley (SW) flows. Three Womersley numbers, *Wo*, of 26, 13, 5 and one constant Reynolds number (Re = 1440) based on the friction velocity and pipe diameter were investigated. The results indicated that the oscillatory flows relaminarize or reach a conditionally or fully turbulence state depending on *Wo*. The peak of rates decreases with increasing *Wo*. For high *Wo* there was no instabilities found near to the wall. Instabilities were also not detected as the turbulence intensity was increasing during the deceleration phase of the flow or when laminarization happened in acceleration phase for *Wo* = 13. There was also a study about heat transfer within the developing and fully developed periodic flow across porous media (Davari and Maerefat, 2016). The effects of parameters such as baffle height, baffle spacing, Reynolds number and thermal conductivity were investigated. The results showed that the local Nusselt number in the entrance region would be less than that of the fully developed region because the porous baffles cause formation of recirculation zone. The fluid reported in the study of Davari and Maerefat (2016) flows in one direction (i.e. not oscillatory flow) across the porous structure. It is expected that should the fluid flow conditions changes, the fluid dynamics across the porous structure should change too. Clearly, the understanding of fluid dynamics within the entrance and developing region is important for all types of flow. In this paper, the fluid dynamics behavior within a channel of a porous structure of a 'stack' for thermoacoustic system is investigated with emphasize

on the entrance and/exit regions behavior as flow oscillates across the structure at two different flow frequencies.

2. Methodology

2.1. Computational model

The investigations were done using computational models solved in ANSYS Fluent. A two-dimensional Computational Fluid Dynamic (CFD) model was solved for oscillatory flow conditions across parallel-plate structure that was placed at a location of 0.18λ from the location of pressure antinode. The term λ is the wavelength which is defined as the ratio between the speed of sound, c, and the flow frequency, f (i.e. $\lambda = c/f$). Fig. 2 illustrates the two-dimensional computational domain and its location in the quarter wavelength standing-wave experimental setup (Mohd Saat et al., 2019). The domain was modeled as a rectangular domain with a length of 600 mm and a height of 150 mm. The parallel-plate structure is placed at the center of the computational domain and a point 'm' is also shown at a location within a channel between the two plates, as can be seen on the bottom right side of Fig. 2. The point represents the location where most data are collected for further analysis. This point will be mentioned again in the next section. The models were solved for two different flow frequencies of 14.2 Hz and 23.6 Hz. The frequencies were set following the resulting resonance frequency as measured in the experiment [30]. The working fluid is air that was treated as an ideal gas at an atmosphere pressure. Following the findings as reported in (Mohd Saat and Jaworski, 2017), an SST k-ω turbulence model was used for this investigation. The total number of parallel-plates (stack) are 16 each with 200 mm length and thickness of d = 3 mm. The plates are made from aluminum and they are arranged with a gap of D = 6 mm between the plates.

The boundary conditions for the computational domain were calculated using Thermoacoustic Linear Equation (Swift, 2002; Rott, 1980). The theoretical lossless equations were based on the implementation of oscillating wave behaviour on the standard Navier-Stokes equation. The oscillating wave behaviour is represented by harmonic oscillations of density, ρ, pressure, p, and velocity, u:

$$\rho = \rho_m + Re\left[\rho_1 e^{i\omega t}\right] \tag{1}$$

$$P = P_m + Re\left[P_1 e^{i\omega t}\right] \tag{2}$$

$$u = Re\left[u_1 e^{i\omega t}\right] \tag{3}$$

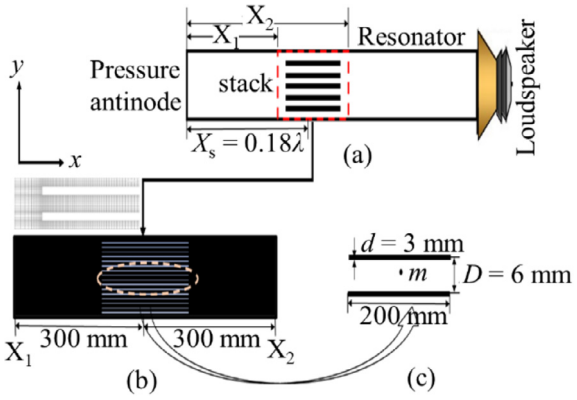

Fig. 2. Computational domain.

The oscillating flow in thermoacoustics should ideally allow no steady gas motion in the absence of acoustic oscillation and hence the velocity is only a function of oscillating time. The complex term $e^{i\omega t}$ is defined as $e^{i\omega t} = \cos(\omega t) + i\sin(\omega t)$ and the term Re is representing real value of the component in the bracket []. The subscripts 'm' and '1' are the mean value and the first order harmonic value, respectively. The inclusion of sound wave flow behaviours as described by Eqs. (1)–(3) into the standard Navier-Stokes Equation (the lossless equation neglects higher order components such as viscous dissipation) lead to the continuity and momentum equations for thermoacoustic environment which can be described as:

$$i\omega\rho_1 + \rho_m \frac{\partial u_1}{\partial x} = 0 \tag{4}$$

$$i\omega\rho_m u_1 = -\frac{dP_1}{dx} \tag{5}$$

For ordinary sound wave that propagates through a channel, the speed of sound is given by $c = \sqrt{(\partial p/\partial\rho)_s}$ where p is the pressure, ρ is the density and s represents isentropic process of the sound propagation. The fast travel of the sound wave can be approximated as an isentropic process. As a result, the continuity and momentum equation for lossless model can be shown to be:

$$i\omega P_1 = -\rho_m c^2 \frac{\partial u_1}{\partial x} \tag{6}$$

$$i\omega u_1 = -\frac{1}{\rho_m}\frac{\partial P_1}{\partial x} \tag{7}$$

The general solution for u_1 and p_1 for sinusoidal periodic flow in the channel can be represented as $C\cos k_a(x - x_0)$. The term k_a is the wave number defined as $k_a = \omega/c$ with $\omega = 2\pi f$ as the angular velocity as a function of flow frequency, f, and c is the speed of sound. For a special case of standing wave situation, a hard end is applied at the one end of the test rig ($x = l$) which is known as the pressure antinode location if the rig is having a length equal to a quarter of the wavelength of air. At the location of the hard end, the velocity is zero. Hence the solution can be shown to be:

$$P_1 = C\cos k(x - l) \tag{8}$$

The amplitude of the constant C depends on the applied force on the flow at the other end of the rig (i.e. the location of the acoustic driver). The experimental practice showed that the applied force is related to the change of pressure at the hard end (pressure antinode) and this can be monitored experimentally by using a pressure sensor. This amplitude of pressure at the location of pressure antinode is denoted as P_a. By applying Eq. (8) with $C = P_a$ to calculate for the oscillating pressure amplitude, an oscillatory pressure value was assigned as inlet boundary condition (at location x_1) by using equation $P_1 = P_a cos(k_a x_1) cos(2\pi ft)$.

A theoretical equation for oscillating velocity, u_1, can be obtained by applying the solution for the oscillating pressure amplitude into the lossless momentum equation given by Eq. (7). Velocity is related to mass flux by a relationship of $m' = \rho u_1$. An oscillating mass flux was defined as outlet boundary condition (at location of x_2) and the mass flux was defined as $m_2' = \frac{P_a}{c} sin(k_a x_2) cos(2\pi ft + \theta)$. The terms $P_a, c, k_a, f, t, \theta, x_1 and\ x_2$ are acoustic pressure at the location of pressure antinode (P_a), speed of sound, wavenumber, flow frequency, time, phase angle between pressure and velocity and the location of the inlet and outlet boundaries of the computational domain with respect to the hard end of the resonator, respectively.

Two additional boundary conditions for turbulence model were assigned as the turbulent length scale, $\ell = 0.07D$, and the turbulent

intensity, $TI = 0.16(Re)^{-1/8}$. Quadrilateral type of mesh was used in this model. The computational domain was divided into several parts to improve the quality of mesh. The meshes used for the simulations were with maximum skewness of 0.053 and a maximum aspect ratio of 38.4. The minimum orthogonal of 0.94 was recorded. The model was solved using transient pressure-based implicit solver with the applications of the Pressure-Implicit with Splitting Operators (PISO) scheme for the pressure–velocity coupling. The spatial discretization method and a least-squares cells-based method were selected for gradient and a second order upwind scheme was used for the pressure, density, momentum, and turbulent kinetic energy calculations. Independency test was done and the cells number of 106,000 was found sufficient to provide solution that is insensitive to grid size. Transient models were applied with time step size of 1/1200*f* so that enough calculations (between 10 and 20) are done before convergence is achieved in every time step. The models were solved for a minimum of seven cycles each. This is to ensure a steady oscillatory flow condition is achieved where the hydrodynamic behaviour of flow is not changing from one cycle to another.

2.2. Model validation and verification

The CFD model was validated using experimental data obtained from an experimental rig as reported by Mohd Saat et al., (2019). The rig is as shown in the top most part of Fig. 3. In brief, the experimental rig was build using a loudspeaker as an acoustic driver that drives sound wave inside the resonator that was attached to it. The resonator is a straight chamber with length of 6.60 m for 14.2 Hz frequency and 3.80 m for 23.6 Hz frequency. The cross-sectional area of the resonator is 150 mm × 150 mm. The resonator was built with several segments that will allow the alteration of the total length and the arrangement of location of test section to suit the investigated resonance frequency of the rig. Two arrangements and total lengths were used to obtain results for two different flow frequencies of 14.2 Hz and 23.6 Hz. The schematic diagram of the two arrangements are as shown in the middle and bottom parts of Fig. 3.

The power input to the loudspeaker (PD1860) was controlled using an amplifier (FLP-MT 1201) and a voltage generator (SG1005). At the hard end of the resonator, known as the location of pressure antinode, a piezoresistive pressure sensor (Endevco 8510B-2) was flush mounted on that surface and value of pressure amplitude was recorded to monitor the flow inside the resonator. The voltage input of the pressure sensor was controlled using a voltage supply to avoid failure of sensor due to oversupply of input voltage. The pressure sensor was then connected to a datalogger (DI-718B) and a computer. The data from the sensor was processed using a Windaq software that is compatible with the datalogger used in this study. In addition to that, a hotwire (ST732) was placed at locations around the 'test section' and the collected data are used for validating the CFD models. The validation was done by comparing experimental data and CFD data at exactly the same location of 120 mm measured from the end of the 'stack' structure. The results of the validation are as shown in Fig. 4.

The dimensionless form of velocity is used to represent the data of velocity amplitude change with drive ratio. In thermoacoustics, the amplitude of flow is normally presented using a term known as drive ratio, Dr. The drive ratio, Dr, is defined as the ratio of pressure amplitude at the location of pressure antinode, P_a, and the mean pressure, P_m. Drive ratio changes with the change of flow amplitude. The values of drive ratio and its corresponding Reynolds number for all investigated cases presented in this paper is listed in Table 1 as reference. The Reynolds number shown in this table is calculated using the amplitude of velocity at the inlet.

The results from CFD model were also verified using theoretical formula. The lossless theoretical formula as shown in earlier sections were improved by an introduction of a two-dimensional impact of the flow domain as presented by a term known as a 'shape factor', h_v (Swift, 2002). Hence, the velocity amplitude can be calculated as:

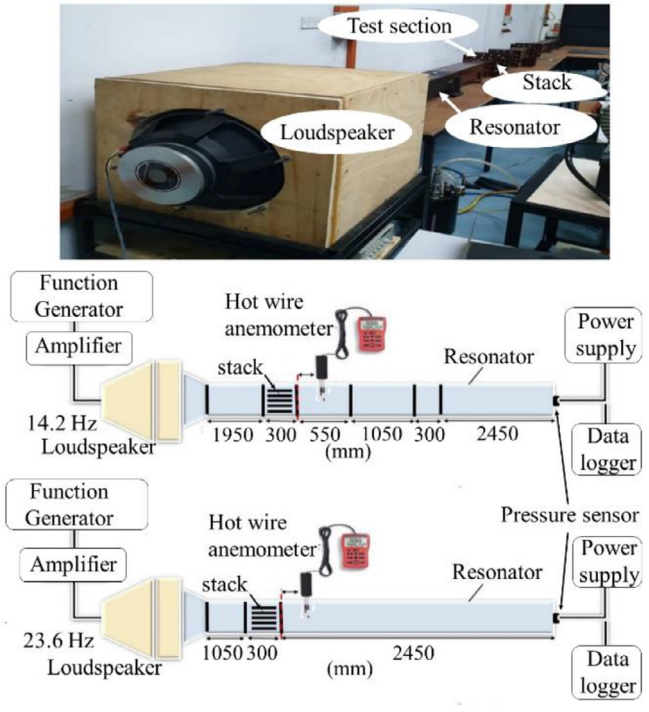

Fig. 3. A real picture of the experimental rig (top), the schematic diagram of 14.2 Hz rig (middle) and the schematic diagram of 23.6 Hz rig (bottom).

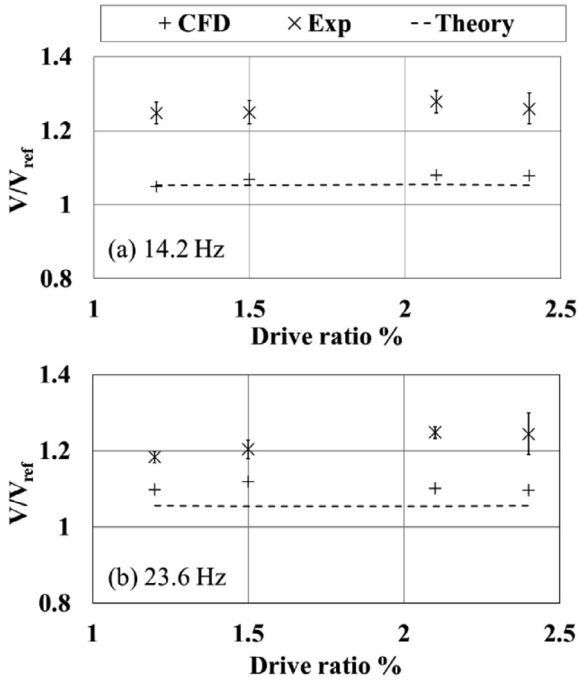

Fig. 4. Validation of CFD model with comparison to experimental and theoretical data.

Table 1
Drive ratio and Reynolds number for all investigated cases.

Drive ratio %	Reynolds number	
	14.2 Hz	23.6 Hz
0.3	6290	5936
0.83	17,409	16,424
1.5	31,463	29,682
2.1	44,048	41,555
3	62,926	59,364

$$u = \frac{k.p_a sin(kx)}{\varnothing \omega \rho_m} sin(\omega t).Re[1 - h_v] + \frac{k.p_a sin(kx)}{\varnothing \omega \rho_m} cos(\omega t).Im[1 - h_v] \quad (9)$$

where $k, p_a, \varnothing, \omega, \rho_m$ are the wave number, pressure amplitude at the location of pressure antinode (Pa), porosity (area of the air divided by the total area), angular frequency, and the mean density of the working fluid. The terms 'Re' and 'Im' represent the real and imaginary parts of the calculation. The shape factor, for the parallel-plates of the channel, h_v, is defined as (Swift, 2002):

$$h_v = \frac{cosh[(1+i)y/\delta_v]}{cosh[(1+i)y_0/\delta_v]} \quad (10)$$

where y ,y_0 andδ_v present the space between the plates (mm), central location of the spacing (mm) and viscous penetration depth (mm), respectively.

The comparison between experiment, CFD and theory is done for data taken at a similar location which is 120 mm from the end of the stack. These values were made dimensionless using a reference value of velocity. The reference velocity, V_{ref}, was theoretically calculated using inlet boundary condition of the computational domain. The value changes depending on drive ratio. Table 2 shows the values of V_{ref} for all cases of drive ratios used in this study.

The validation results shown in Fig. 4 show that the CFD results fall within the range as predicted theoretically and as measured experimentally. The experimental data are presented with error bars that represent the uncertainties of experimental values. The uncertainties were calculated using standard deviation technique for data collection. It must be noted that all results were made dimensionless by using theoretical reference velocity. Hence, the difference shown in Fig. 4 is the difference relative to theoretical values. The experimental data is bigger than the data provided by CFD by approximately 17% for frequency of 14.2 Hz and by 11% for frequency of 23.6 Hz. The differences may be due to the three-dimensional effect that was not considered in the model.

For transient case, solving a three-dimensional model is challenging and time-consuming. Hence, the use of Reynolds-averaged model with two-dimensional approximation is usually computationally more sensible (Yamanaka et al., 2002). Interestingly, the pattern of CFD results are the same with the pattern showed by experimental data. The theoretical calculation predicts that the velocity does not change much with locations, hence the value is near unity. This is not the case shown by the experimental results. The differences in magnitude of velocity may be related to the presence of vortex at the end of that structure (Harikumara et al., 2019; Yamanaka et al., 2002). It is clear, however, that the CFD models provide results that are closer to experiment if compared to the theoretical prediction. Similar pattern of velocity amplitude change with the change of drive ratio indicating that the model did captured the feature of the oscillatory flow, even if not all are well captured. Further investigations are definitely needed to mimic the exact behavior of the experimental results. Nevertheless, the similar pattern of velocity change and magnitude that falls within the range of experimental and theoretical results, as observed from the current model, is found sufficient to provide an insight into the fluid dynamics of flow within the 'stack' of thermoacoustics.

Due to the limitation of the experimental rig setup, data for some range of Reynolds could not be obtained experimentally. In this case, the CFD results are verified by comparison to theoretical calculation. The comparison of dimensionless velocity amplitude between CFD and theory is as shown in Fig. 5. The results are shown for Reynolds number ranging from 5936 to 62926. The Reynolds number is calculated using the size of gap at the entrance flow (resonator height), D = 150 mm, as the characteristic length and the velocity amplitude at the reference point, V_{ref}, was used to represent the flow amplitude. The density and viscosity of air are taken at a room temperature of 30 °C.

Oscillatory flow is a cyclic nature of flow. The fluid oscillates across structure in forward and backward movements that change with time. In this paper, the results are reported for twenty phases and the data are recorded at point 'm' as presented earlier in Fig. 2. The twenty phases of the time history data are labelled as Φ1 to Φ20, over a flow cycle.

Fig. 6 shows an example of changes of flow amplitude in one flow cycle for a case with frequency of 14.2 Hz and a drive ratio of 1.5%. The twenty phases represent the acceleration and deceleration stages during the forward (+ve amplitude) and backward (-ve amplitude) movements. The difference in magnitude value from CFD and theory is consistent with results shown in Fig. 4 and Fig. 5 and are expected to be due to the additional features of vortex which may not be well captured by the theoretical linear equation.

The oscillatory flow across the parallel-plate structure results in interesting behavior of flow within the channel especially at locations near both ends of the structure. The results are presented in the next sections.

Table 2
Velocity reference V_{ref} for investigated drive ratios with flow frequency of 14.2 Hz and 23.6 Hz.

Drive ratio %	Velocity reference V_{ref}	
	14.2 Hz	23.6 Hz
0.3	0.62692	0.59144
0.83	1.73449	1.636316
1.2	2.50769	2.365758
1.5	3.13462	2.957198
2.1	4.38847	4.140077
2.4	5.01539	4.731517
3	6.26924	5.914396

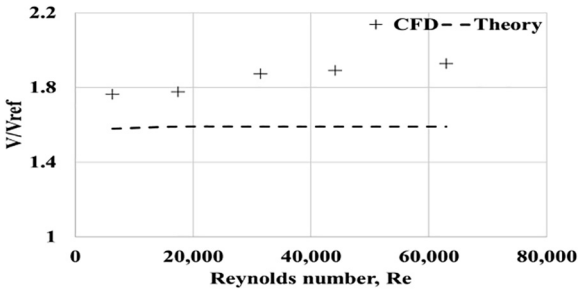

Fig. 5. Variation of dimensionless velocity, V/Vref, over the range of investigated Reynolds number.

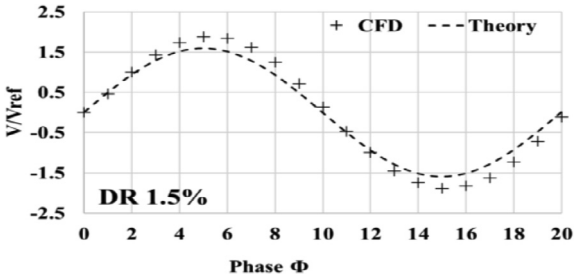

Fig. 6. Changes of dimensionless velocity (V/V_{ref}) with phases change in one flow cycle for frequency of 14.2 Hz.

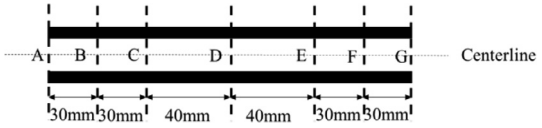

Fig. 7. Centerline and locations of vertical lines for data presentation along the channel.

3. Entrance/exit region investigation

Investigation of the entrance region of an oscillatory flow within the channel will be presented in two ways; through plots of velocity amplitude at the centerline of the channel and the velocity profiles plotted at several locations along the channel. The locations are defined as **A**, **B**, **C**, **D**, **E**, **F** and **G** as are shown in Fig. 7. Results are to be shown for three phases during the first half of the cycle: Φ3, Φ5 and Φ8. Results are presented for two different drive ratio of 0.83% and 3%.

3.1. Velocity profiles within the channel

This section presents the velocity profiles within the channel at frequencies of 14.2 Hz and 23.6 Hz. The results are shown only for first half of the flow cycle (when the fluid flows forward). Axial velocity profiles were plotted at locations **A** to **G**as defined earlier in Fig. 7. Locations **A** and **G** are located exactly at the ends of the plates. Three phases that represent different stages of an oscillatory flow within the first half of the cycle were selected. The phases are Φ3 (at acceleration stage), Φ5 (at the maximum velocity amplitude) and Φ8 (at deceleration stage). Fig. 8 illustrates the velocity profiles for 0.83% drive ratio for both frequencies.

The results show that there are three different types of velocity profiles formed within the channel. At phase Φ3 for both frequencies, an 'm' shape velocity profile was seen for all the defined locations. An 'm' shape velocity profiles represent the situation where maximum velocity amplitude is not at the center of the channel but at locations away from the center towards the solid wall. There is a slight difference in the pattern of velocity profiles if comparison is made between results for both flow frequencies. This minor difference may be related to the change of boundary layer near the wall and the impact of the rapidness of flow as frequency increases. At the end of the channel (labelled as **G**) the velocity profiles at Φ8 for low flow frequency (left plots) appeared in a form of a curve. This represents a parabolic-like profile with maximum amplitude of velocity happens at the center of the channel.

For high frequency (right plots) the velocity profiles exhibited a feature of almost a vertical line at the center of the channel. This resembles a 'slug-like' profile that represents uniform temperature at the center of the channel. It is also observed that the velocity profiles of flow with frequency of 23.6 Hz is symmetrical with respect to the centerline of the channel. For low frequency of 14.2 Hz, some asymmetrical features are found particularly at the entrance location of **A** in phases Φ3 and Φ5. The two phases are representing the acceleration phase of the forward flow and Φ5 is the peak of that phase. As the flow decelerates at Φ8, the asymmetrical feature is not anymore seen. It seems that for low drive ratio of 0.83% (a drive ratio below 1%), asymmetrical profile of velocity was detected at the entrance of the channel if the flow frequency is low. This may be related to the combined effect of the low flow amplitude (low drive ratio) and a slower pace of flow (low frequency). The values of velocities at all locations for low flow fre-

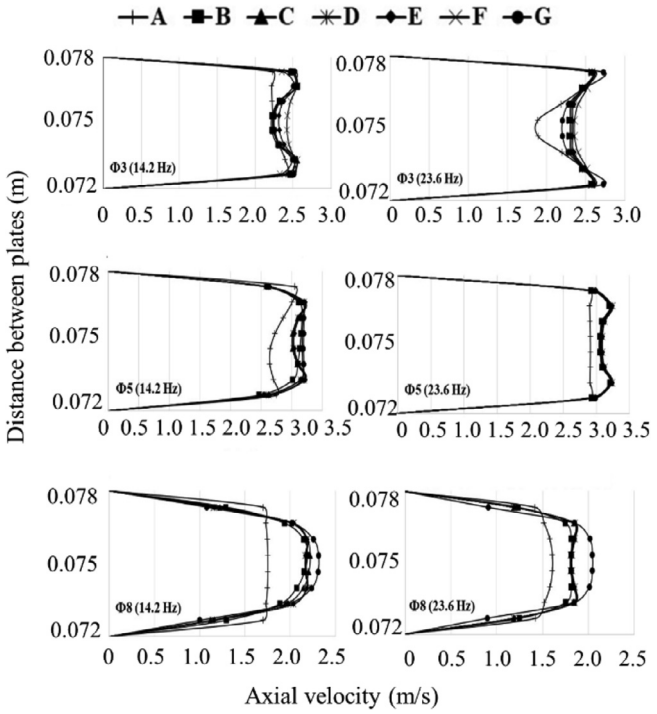

Fig. 8. Velocity profiles at several locations inside the channel for 0.83% drive ratio at low frequency of 14.2 Hz (left) and 23.6 Hz (right).

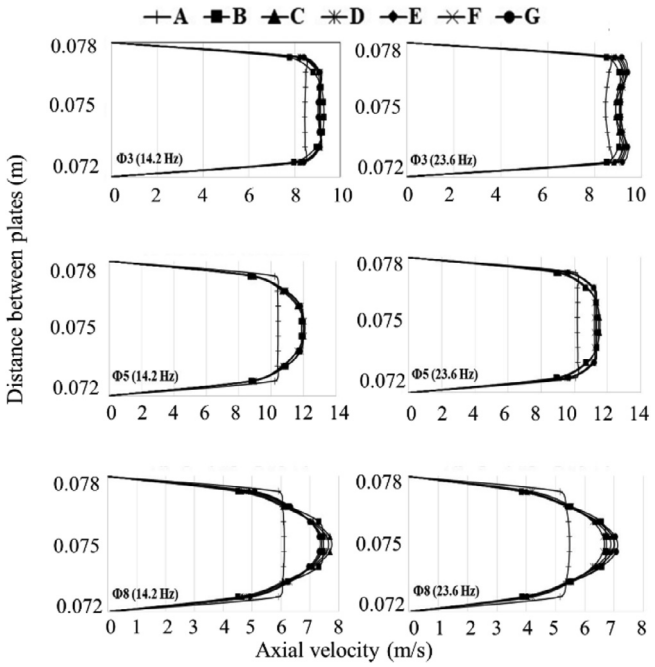

Fig. 9. Velocity profiles at several locations inside the channel for 3% drive ratio at low frequency of 14.2 Hz (left) and 23.6 Hz (right).

quency are slightly higher than that for high flow frequency. This indicates that the fluid oscillates to a slightly larger distance when the flow frequency is lower.

Fig. 9 shows the velocity profiles at a higher drive ratio of 3% for both flow frequencies. For low velocity amplitude at phase Φ3, an 'm' shape velocity profiles appeared strong at high flow frequency. A shape that almost resembles an 'm-shape' profile is also seen at location **G** of the low frequency, but it looks more like a 'slug-like' profile. Location **G** is the exit/entrance point located at the right side of the parallel-plate structure. Hence, the presence of 'm-shape' profile at this location during phase Φ3 may be related to the remaining impact or the residual of momentum of the reversed flow that may still be felt by the fluid at that location as the flow starts to change its direction forward.

The changes of velocity amplitude at the middle locations of the channel is very small, if any. But it is interesting to note that there is a change of shape of velocity profile at the middle locations of the channel (locations **C**, **D**, **E**) as the flow changes from Φ3 to Φ8. At low drive ratio, as shown in Fig. 8, the velocity profiles at the middle locations (locations **C**, **D**, **E**) retain a shape that resembles an 'm-like profile' for all Φ3, Φ5 and Φ8. However, at high drive ratio (Fig. 9) the shape of velocity profiles changes from 'm-like' at the acceleration stage, to a 'slug-like' profile at the maximum peak of Φ5 and then a 'parabolic-like' profile during the deceleration stage. The change of velocity profile for high drive ratio indicates a strong influence of entrance effects on flow inside the channel.

It is also noted that asymmetrical feature that was observed for low frequency of low drive ratio (c.f. Φ1 and Φ5 on the left side of Fig. 8) is not anymore seen in the velocity profile of the flow at high drive ratio (Fig. 9). At high drive ratio, the amplitude of flow is high, hence the mean flow enters the channel with stronger momentum leading towards a more symmetrical feature of velocity profile including at the entrance location of the channel.

Comparison between the left and right sides of velocity plots in Fig. 9 shows that the development of velocity profiles (from phase Φ1 to Φ8) are almost similar for both flow frequencies. This indicates that the impact of flow frequency on velocity profile within the channel is not very prominent as the drive ratio increases. Again, the velocity amplitude of flow at lower frequency is slightly higher than that of the high frequency, hence the fluid flows to a slightly larger distance when the flow frequency is lower.

3.2. 'Entrance' and 'Exit' effects within the channel

In this section the axial velocity amplitude was plotted at the centreline of the channel to investigate the influence of the entrance/exit region. For oscillatory flow, the fluid oscillates across the porous structure. This means that the fluid flows forward and backword in a cyclic manner that depends on the flow frequency. As a result, both ends of the channel become the entrance region and exit region depending on the phase of the flow. During the first half of the cycle, the fluid flows forward as declared in Fig. 6. Hence, the left side of the channel acts as entrance for flow at phases Φ1 to Φ10. In the second half of the cycle, fluid reverses. Therefore, the left side of the channel now becomes the exit region as the fluid enters from the right side of the channel. In Fig. 10, the results of the centerline velocity amplitudes for a drive ratio of 0.83% are plotted for several phases. The *x*-axis represents the location of the channel/plates within the computational domain. The results are shown for the entire length of plate for one flow channel. Hence the minimum value of *x*-axis represents the left end of the channel while the maximum value of the *x*-axis is the right end of the channel. The channel is 200 mm long.

The centreline velocity shown in Fig. 10 is for flow with drive ratio of 0.83%. The left plots are for the low flow frequency of 14.2 Hz and the plots on the right side of the figure is for flow frequency of 23.6 Hz. Four phases of flow were selected from both flow frequencies models: phase Φ1, phase Φ3 (at acceleration stage), phase Φ5 (at the peak of acceleration stage) and phase Φ8 (at deceleration stage). Results are also shown for phases Φ11, Φ13, Φ15 and Φ18 when the flow reverses. The black solid line presents results for flow during forward direction (the direction of flow is from the left to the right side). The orange solid line represents the flow when it is reversed (the fluid flows in the direction from the right to the left side).

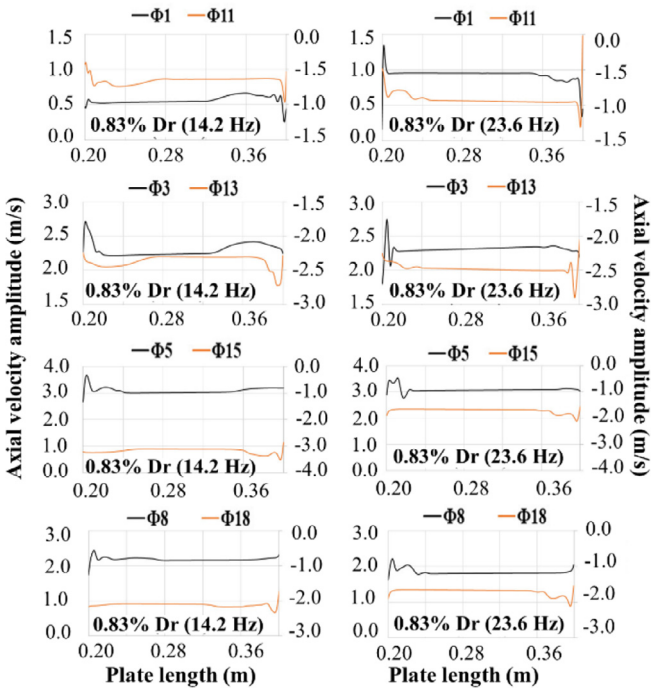

Fig. 10. Velocity amplitude at centerline of the channel for 0.83% drive ratio for low flow frequency (left) and higher flow frequency (right).

At phase Φ1, the amplitude of flow is small. The fluid is about to start its flow from the left end. This is indicated by a positive spike in the velocity amplitude value at the beginning of the *x*-axis. During the first half of the cycle (Φ1 to Φ10) the location of x = 0.2 is known as the 'entrance' while the location of $\times$ = 0.4 is known as the 'exit'. The momentum of flow from previous cycle is still felt by the flow within the channel, particularly near the exit of the channel. This is seen as the fluctuation of velocity amplitude at locations near the right end of the *x*-axis.

Comparison of velocity values between the left and right ends indicates that the fluctuation of velocity values at the 'exit region' is stronger compared to that at the 'entrance region'. The 'exit region' is also bigger compared to the 'entrance region'. For the low frequency of 14.2 Hz, the 'exit effect' is felt by the fluid within the length of 80 mm from the right end. The 'entrance effect' at this phase is only affecting the fluid within the length of about 10 mm from the left end. As the flow amplitude increases in phases Φ3 and Φ5, the length of the 'entrance region' becomes higher while the 'exit region' is shorter. As the fluid decelerates at Φ8, the fluctuation of velocity at the 'entrance' can be seen up until the location of 80 mm from the inlet while the 'exit effect' seems disappearing. The same pattern is seen for flow at a higher frequency of the 23.6 Hz but the lengths of areas affected by the 'entrance' and 'exit' effects are smaller compared to that of the low flow frequency. As the fluid reverses (phases Φ11, Φ13, Φ15 and Φ18), the entrance location changes to the right side of the channel and the left side becomes the exit. Almost a symmetrical profile of

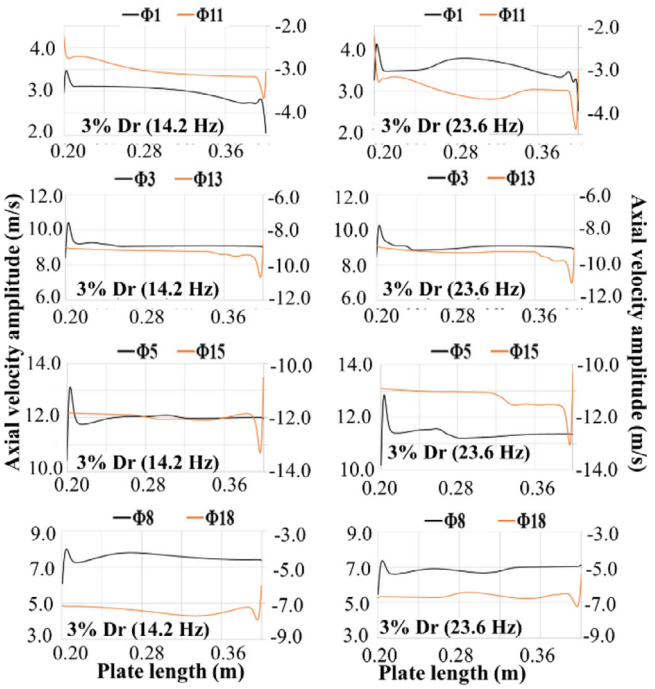

Fig. 11. Velocity amplitude at centerline of the channel for 3% drive ratio for both flow frequencies.

centreline flow amplitude is seen between the forward and reversed directions of flow.

Fig. 11 illustrates the change in centerline velocity amplitude along the channel for flow with higher drive ratio of 3% at frequencies of 14.2 Hz and 23.6 Hz. Generally, for both frequencies the areas affected by 'entrance effect' increases as drive ratio increases. The 'exit region' seems disappeared especially at phases from Φ3, Φ13, Φ5 and Φ15 for both flow directions. This is judged by the absence of fluctuation or peak of velocity amplitude at the exit of the channel. At Φ8 and Φ18, when the flow is decelerating, changes in velocity amplitude values can be seen throughout the channel. It is hard to find a region with fully developed behaviour of flow. The amplitude of velocity seems changing at almost all locations within the channel and this happens for almost all the phases of flow. This is happening due to the large flow amplitude at high drive ratio.

A symmetrical pattern of velocity amplitude between the forward and backward flow directions was observed for both flow frequencies. The velocity amplitude profile is also symmetrical with respect to the center of the channel. This indicates similar or symmetrical flow behavior of entrance and exit regions as drive ratio increases.

The axial velocity, V, is related to the gas displacement amplitude,δ, via a relationship of $V = \omega\delta$where the angular velocity,ω, is a function of flow frequency $\omega = 2\pi f$. Hence, a higher value of velocity indicates that the fluid flows to a larger distance within the channel. As a result, the entrance region should be bigger as drive ratio increases. Since flow frequency is also affecting the gas displacement amplitude, the entrance region will be affected by the flow frequency as well. Comparison between results of Fig. 10 and Fig. 11 shows that at a low flow amplitude of 14.2 Hz the entrance region extends to a larger distance into the channel when the drive ratio increases from 0.83% to 3%.

In order to look closely at the 'entrance' and 'exit' impacts on the flow within the channel, the results of centerline velocity are presented with comparison to the amplitude of axial velocity at the center of the channel (x = 0.3 m). This is done by introducing a dimensionless parameter of velocity defined as:

$$\frac{|V| - |V_{x=0.3m}|}{V_{ref}} \tag{11}$$

The changes of velocity along the channel are observed through the difference between the absolute value of the centerline velocity of all the cases, $|V|$, and the absolute value of axial velocity at the center of the channel $|V_{x=0.3m}|$. The sign of velocity (direction of flow) is neglected by considering this absolute value. This is done to focus on the difference between the velocity amplitude at other locations to the location at the center of the channel. Ideally, if a fully developed flow is achieved within the channel, then the differences between $|V|$ and$|V_{x=0.3m}|$ should be consistently the same. Else, the flow is defined as developing flow. The velocity values are made dimensionless using reference velocity as listed earlier in Table 2. The results are shown in Figs. 12 and 13.

The results of Figs. 12 and 13 are shown for all the twenty phases of a flow cycle. The plots on the left side of the figures are for the first half of the cycle (Φ1 to Φ10) and the plots on the right side of the figures are for the second half of the cycle (Φ11 to Φ20). Results are also shown for different cases of drive ratio starting from the lowest on top and the highest at the bottom of both Figs. 12 and 13. The dimensionless velocity changes for flow frequency of 14.2 Hz are presented in Fig. 12 while Fig. 13 shows the results for the higher flow frequency of 23.6 Hz.

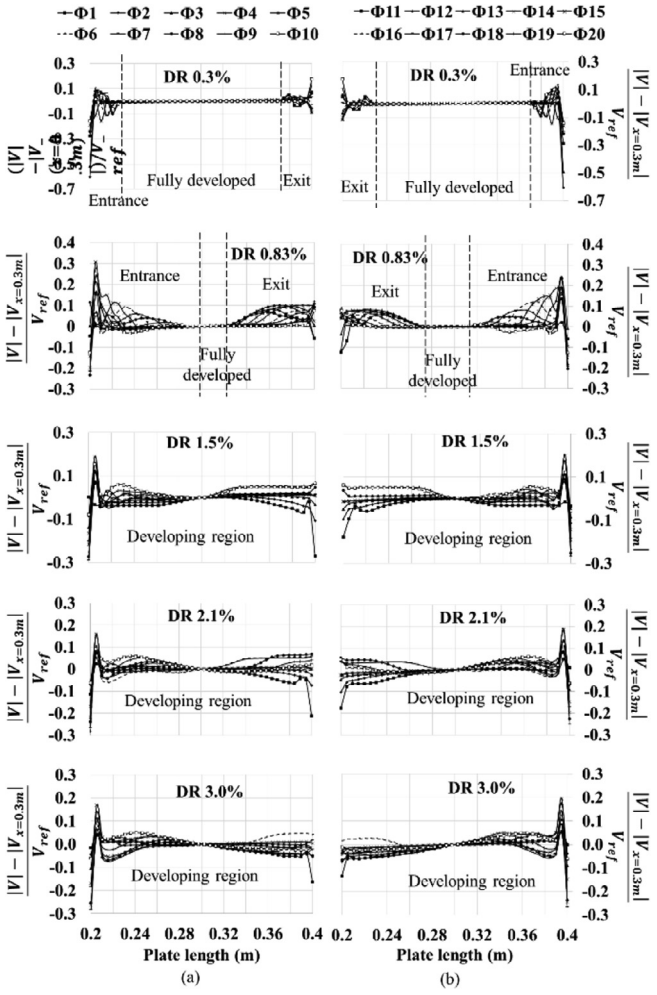

Fig. 12. Centerline velocity for flow frequency of 14.2 Hz during (a) first half of the cycle and (b) second half of the cycle.

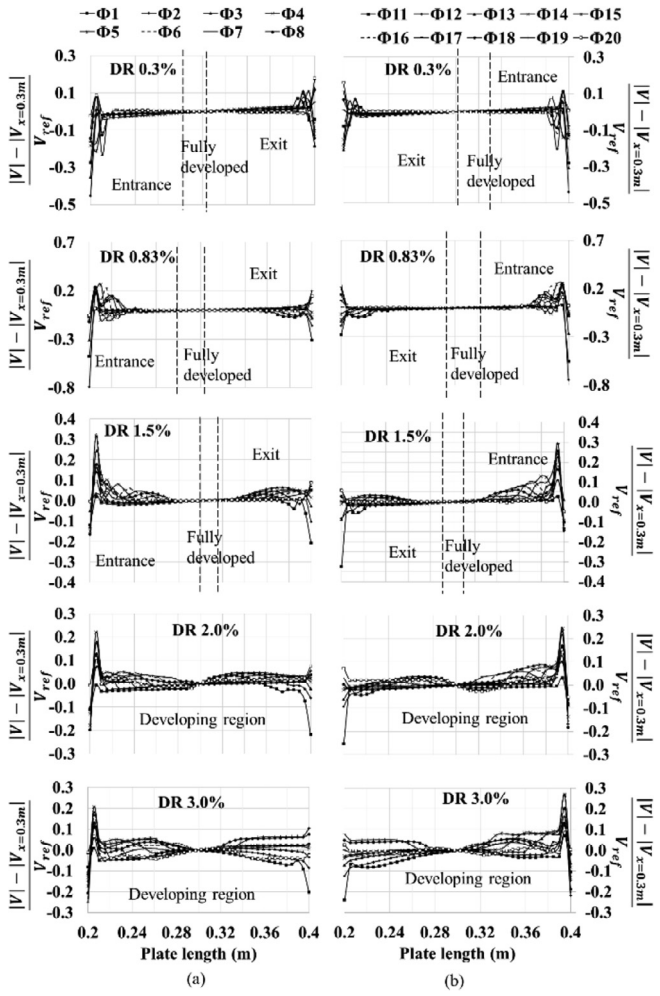

Fig. 13. Centerline velocity for flow frequency of 23.6 Hz during (a) first half of the cycle and (b) second half of the cycle.

At low flow frequency, features of fully developed region are noticed at the middle locations of the channel for flow with low range drive ratio of 0.3% and 0.83%. As drive ratio increases, velocity changes can be seen happening throughout the channel. This indicates that the flow within the channel is developing throughout the cycle. This is consistent with results shown in Fig. 8 and Fig. 9. In Fig. 8, the velocity profiles at the middle locations of **C**, **D** and **E** resemble an 'm-like' profile for phases Φ1, Φ5 and Φ8. Similar shape of profile indicates that the flow within the middle of the channel can be considered as fully developed at low drive ratio of 0.83%. At higher drive ratio of 3%, as earlier shown in Fig. 9, the velocity at locations **C**, **D** and **E** changes from 'm-like' profile at Φ1 to a 'slug-like' profile at Φ5 and a 'parabolic-like' profile at Φ8. This change of velocity profiles happening at high drive ratio of 3% indicates that the flow in the channel is developing even at the middle locations of the channel.

As expected, a symmetrical feature of entrance and exit regions are observed at both ends of the channel between the forward flow (left) and backward flow (right) conditions. The symmetrical feature between forward and backward flow conditions are also seen as flow frequency increases. However, it is interesting to note that the fully developed region of flow can still be detected at a drive ratio of 1.5% when fluid flows with frequency of 23.6 Hz (Fig. 13). This is consistent with the results shown earlier, where higher flow frequency leads to a slightly shorter travel of fluid particles. As a result, the fully developed flow feature can still be observed at drive ratio of 1.5%. At higher drive ratio of 2.1% and 3%, the fluid inside the channel exhibits developing flow characteristics for the entire length of the channel.

It is also interesting to note that the 'entrance' and 'exit' effects can be seen during both directions of flow; forward flow (Φ1 to Φ10) and backward flow (Φ11 to Φ20). This is indicated by the presence of peaks of dimensionless velocity amplitude at both ends of the channel. Hence, for oscillatory flow, the results show that the 'entrance' and 'exit' effects are influencing the fluid dynamics of flow regardless of the direction of flow. This leads to the existence of 'entrance' and 'exit' regions within the channel during the cyclic flow of gaseous across the parallel-plate structure of a standing wave thermoacoustic environment as investigated in this paper.

4. Conclusion

This paper presents the investigation of the 'entrance' and 'exit' effects on oscillatory flow across a parallel-plate structure of a standing-wave thermoacoustic system. The effects were demonstrated using velocity plots across the channel of a parallel-plate structure. Two-dimensional CFD models were solved and validated with experimental and theoretical data. Three shapes of velocity profiles; the 'm' shape, the 'slug' shape and the 'parabolic' shape profiles, formed within a channel of the parallel-plate structure in different situations depending on drive ratio and frequency of the oscillatory flow. Investigations of velocity change within the channel indicates that there are 'entrance' and 'exit' effects that happened within the channel due to the cyclic nature of the oscillatory flow. Fully developed flow feature was only detected at low drive ratio. Higher flow frequency leads to a shorter travel distance of gas particles, hence fully developed region can be detected at slightly higher drive ratio compared to low frequency oscillatory flow. At higher drive ratio, the flow within the channel is developing throughout the 200 mm length of the investigated structure. The results presented in this paper suggested that developing flow is likely to be the feature of fluid dynamics of an oscillatory flow across a parallel-plate structure as commonly found in most thermoacoustic energy system. Hence the impact of this developing flow on performance of thermoacoustic system should be seriously considered in the future design of the system even if the system is running at low range of Reynolds number.

Declaration of Competing Interest

The authors confirmed that they have no known competing financial interests or personal relationships that could have appeared to influence the work reported in this paper.

Acknowledgements

The authors would like to thank Universiti Teknikal Malaysia Melaka (UTeM) for providing research facilities for this research works.

References

Abdoulla-Latiwish, K.O.A., Jaworski, A.J., 2019. Two-stage travelling wave thermoacoustic electricity generator for rural areas of developing countries. Appl. Acoust. 151, 87–98.

Agarwal, H., Unni, V.R., Akhil, K.T., Ravi, N.T., Sujith, R.I., Pesala, B., 2016. Compact standing wave thermoacoustic generator for power conversion applications. Appl. Acoust. 110, 110–118.

Al-habahbeh, O.M., Mohamad, A., Al-khalidi, A., Khanfer, M., Obeid, M., 2018. Design optimization of a large-scale thermoelectric generator. J. King Saud Univ. Eng. Sci. 30, 177–182.

Avent, A.W., Bowen, C.R., 2015. Principles of thermoacoustic energy harvesting. Eur. Phys. J. Spec. Top. 224 (14–15), 2967–2992.
Berson, A., Michard, M., Blanc-Benon, P., 2008. Measurement of acoustic velocity in the stack of a thermoacoustic refrigerator using particle image velocimetry. Heat Mass Transfer 2008, 1015–1023.
Brown, S.J., Domanski, P.A., 2014. Review of alternative cooling technologies. Appl. Therm. Eng. 64, 252–262.
Davari, A., Maerefat, M., 2016. Numerical analysis of fluid flow and heat transfer in entrance and fully developed regions of a channel with porous baffles. J. Heat Trans. 138, (6) 062601.
Dombrowski, N., Foumeny, E.A., Ookawara, S., Riza, A., 1993. The influence of Reynolds number on the entry length and pressure drop for laminar pipe flow. Can. J. Chem. 71 (3), 472–476. https://doi.org/10.1002/cjce.5450710320.
Feldmann, D., Wagner, C., 2012. Direct numerical simulation of fully developed turbulent and oscillatory pipe flows. J. Turbul. 13, N32.
Friedmann, M., Gillis, J., Liron, N., 1968. Laminar flow in a pipe at low and moderate reynolds numbers. Appl. Sci. Res. 19, 426–438.
Fu, H.L., Leong, K.C., Huang, X.Y., Liu, C.Y., 2001. An experimental study of heat transfer of a porous channel subjected to oscillating flow. J. Heat Trans. 123 (1), 162–170. https://doi.org/10.1115/1.1336510.
Gallego, E., Rubio-Clemente, A., Pineda, J., Velasquez, L., Chica, E. 2020. Experimental analysis on the performance of a pico-hydro Turgo turbine. J. King Saud Univ. Eng. Sci.
Gerrard, J.H., Hughes, M.D., 1971. The flow due to an oscillating piston in a cylindrical tube: A comparison between experiment and a simple entrance flow theory. J. Fluid Mech. 50 (1), 97–106. https://doi.org/10.1017/S0022112071002477.
Gillis, J., Brandt, A., 1966. Magnetohydrodynamic flow in the inlet region of a straight channel. Phys. Fluids 9, 690–699.
Han, L.S., 1960. Hydrodynamic entrance lengths for incompressible laminar flow in rectangular ducts. J. Appl. Mech. 27, 403.
Harikumara, G., Hob, K.H., Wangc, K., Dubeya, S., Duanb, F., 2019. Thermoacoustic energy conversion in a square duct. Energy Procedia 158, 1811–1816.
Homadi, A., Hall, T., Whitman, L., 2020. Using solar energy to generate power through a solar wall. J. King Saud Univ. Eng. Sci. 332, 470–477.
Jaworski, A.J., Mao, X., Mao, X., Yu, Z., 2009. Entrance effects in the channels of the parallel plate stack in oscillatory flow conditions. Exp. Therm. Fluid Sci. 33 (3), 495–502.
Mao, X., Yu, Z., Jaworski, A.J., 2007. Oscillating flow in a parallel-plate stack in a standing wave thermoacoustic resonator: PIV measurements within the entrance region. In: Proceedings of the International Congress on Ultrasonics, p. 1564.
Mazzetti, A., Pret, M.G., Pinarello, G., Celotti, L., Piskacev, M., Cowley, A., 2018. Heat to electricity conversion systems for moon exploration scenarios: A review of space and ground technologies. Acta Astronaut.
Nabavi, M., Siddiqui, K., Dargahi, J., 2008. Measurement of the acoustic velocity field of nonlinear standing waves using the synchronized PIV technique. Exp. Therm. Fluid Sci. no. 33, 123–131.
Mohd Saat, F.A.Z., Jaworski, A.J., 2017. Numerical predictions of early stage turbulence in oscillatory flow across parallel-plate heat exchangers of a thermoacoustic system. Appl. Sci. 7, 673. https://doi.org/10.3390/app7070673.
Mohd Saat, F.A.Z., Johari, D., Mattokit, E., 2019. DeltaE modelling and experimental study of a standing wave thermoacoustic test rig. J. Adv. Res. Fluid Mech. Thermal Sci. 60 (2), 155–165.
Nakamura, M., Machida, K., Shimokawa, K., 2017. A study of thermoacoustic refrigerator. SAE Tech. Pap. 2067–2072. https://doi.org/10.4271/2017-01-0158.
Oviedo-Tolentino, F., Romero-Méndez, R., Hernández-Guerrero, A., Girón-Palomares, B., 2008. Experimental study of fluid flow in the entrance of a sinusoidal channel. Int. J. Heat Fluid Flow 29 (5), 1233–1239.
Rott, N. 1980. Thermoacoustics. In Advances in applied mechanics, vol. 20, pp. 135-175. Elsevier.
Shi, L., Yu, Z., Jaworski, A.J., 2011. Investigation into the Strouhal numbers associated with vortex shedding from parallel-plate thermoacoustic stacks in oscillatory flow conditions. Eur. J. Mech. B Fluids, 206–217.
Swift, G.W., 1988. Thermoacoustic engines. J. Acoust. Soc. Am. 84 (4), 1145–1180.
Swift, G.W., 2002. Thermoacoustics: A Unifying Perspective for Some Engines and Refrigerators. Acoustical Society of America, New York. ch. 4.
Wang, U.L., Longwell, P.A., 1964. Laminar flow in the inlet section of parallel plate. AIChE J. 10, 323–329.
Yamanaka, G., Kikura, H., Takeda, Y., Aritomi, M., 2002. Flow measurement on an oscillating pipe flow near the entrance using the UVP method. Exp. Fluids 32 (2), 212–220. https://doi.org/10.1007/s003480100367.
Yang, R.J., Fu, L.M., Hwang, C.C., 2001. Electroosmotic entry flow in a microchannel. J. Colloid Interface Sci. 244 (1), 173–179. https://doi.org/10.1006/jcis.2001.7847.